Automatic Preoperative Planning of DBS Electrode Placement using Anatomo-Clinical Atlases and Volume of Tissue Activated

Olga Dergachyova · Yulong Zhao · Claire Haegelen · Pierre Jannin · Caroline Essert

Abstract

Purpose Deep brain stimulation (DBS) is a procedure requiring accurate targeting and electrode placement. The two key elements for successful planning are preserving patient safety by ensuring a safe trajectory and creating treatment efficacy through optimal selection of the stimulation point. In this work, we present the first approach of computer-assisted preoperative DBS planning to automatically optimize both the safety of the electrode's trajectory and location of the stimulation point so as to provide the best clinical outcome.

Methods Building upon the findings of previous works focused on electrode trajectory, we added a set of constraints guiding the choice of stimulation point. These took into account retrospective data represented by anatomo-clinical atlases and intersections between the stimulation region and sensitive anatomical structures causing side effects. We implemented our method into automatic preoperative planning software to assess if the algorithm was able to simultaneously optimize electrode trajectory and the stimulation point.

Results Leave-one-out cross-validation on a dataset of 18 cases demonstrated an improvement in the expected outcome when using the new constraints. The distance to critical structures was not reduced. The intersection between the stimulation region and structures sensitive to stimulation was minimized.

Conclusions Introducing these new constraints guided the planning to select locations showing a trend towards symptom improvement, while minimizing the risks of side effects, and there was no cost in terms of trajectory safety.

O. Dergachyova · C. Essert
ICube Laboratory, CNRS, UMR 7357, Université de Strasbourg, Strasbourg, France
E-mail: essert@unistra.fr

O. Dergachyova · Y. Zhao · C. Haegelen · P. Jannin
INSERM, U1099, Rennes, F-35000, France
Université de Rennes 1, LTSI, Rennes, F-35000, France
E-mail: olga.dergachyova@univ-rennes1.fr

C. Haegelen
CHU Rennes, Service de Neurochirurgie, Rennes, F-35000, France

1 Introduction

Many symptoms of neurological disorders resistant to drug therapy, especially motor symptoms such as those in Parkinson's disease, can be treated by deep brain stimulation (DBS). This treatment consists of a surgical intervention where one electrode per hemisphere is placed into a certain nucleus located deep in the brain, *e.g.* the subthalamic nucleus (STN) or globus pallidus internus (GPi), through a hole drilled in the skull. Each electrode is connected to a pacemaker that permanently sends electrical impulses to stimulate the nucleus with a high-frequency signal.

This operation has proven its efficacy for more than 15 years not, yet the preoperative planning stage remains a particularly time consuming and delicate task, which requires high expertise, performed while the patient is awake and already prepared for the intervention with the stereotactic frame fixed on the head. To reduce discomfort for the patient, the procedure needs to be quick. The nucleus to be stimulated is only a few millimeters long, so high targeting accuracy is crucial. The trajectory must be safe and avoid the multiple surrounding vessels and anatomical structures to prevent hemorrhages and side effects that can result from lesions on sensitive tissues. The treatment also has to be effective, *i.e.*, maximize benefits and minimize the side effects caused by stimulating inappropriate regions. Given this context, automatic assistance for trajectory planning provides valuable help designed to quickly define electrode trajectories as well as their tip positions and anticipate outcomes. However, most automatic planning methods proposed so far focused solely on ensuring the safety of the proposed path.

Several approaches have been proposed in the literature to help surgeons in the preoperative decision-making process. Some proposed visualizing tools to present relevant information, such as accessibility maps [28]. Many have tried to automatize the preoperative planning stage of the intervention. The early planning tools of a decade ago involved numerous manual interventions [7,16,23,30,36]. More recently, approaches requiring less interaction have emerged [8,5,31,15,33,34]. Several methods focused on maximizing the distance between the candidate trajectory and surrounding at-risk structures [8,33]. Others accounted for a larger variety of placement rules, classified as hard or soft constraints [5,4,15,34]. Regardless of the method, these approaches have primarily focused on optimizing trajectories, along with feasibility and safety, while simply ensuring that the stimulation point (usually one of the metallic contacts of the electrode) is inside the targeted nucleus without optimizing its exact position within the nucleus.

According to various studies [32,35,19,25] symptom improvement strongly depends on how accurately you target the stimulated brain area. Changing the location of the active contact within or around the nucleus may provide different clinical results, whereas the signal coverage of some brain tissues can also cause severe side effects [9,25,27]. That is why accurately selecting the contact point location proves highly relevant in DBS.

In 2015, Pallavaram *et al.* proposed new integrated software able to automatically suggest a reasonable stimulation location [31]. This location was chosen among the most frequently used clinical active contact positions, based on the segmentation of electrodes from postoperative CT images. In their retrospective study, a point of high probability was defined as a combination of clusters of clinical active contact positions, projected onto the patient's image. However, their proposition of clinical active contact positions appears to be based solely on how often the point was selected by a multidisciplinary surgical team, without considering actual patient outcomes. This method, contrary to the approaches mentioned above, focused solely on selecting the stimulation point, regardless of the trajectory. Earlier, in 2014 the same team reported a retrospective study involving a trajectory planning algorithm algorithm [24] that was quite similar yet with a fixed stimulation point.

In 2012, Bériault *et al.* proposed an approach integrating a model of the DBS electric field from multiple active contacts [6]. Their planning approach was based on computing the optimal intensity allowing for the best possible coverage of the targeted anatomical structure by the stimulated volume, while avoiding a patient-specific side-effect area (such as internal capsule). In that work, the electrode tip position was fixed beforehand.

In our previous works, we introduced a fully modular geometric constraint solving approach for preoperative trajectory planning. This enables easy writing, updating or extending of the multiple constraints used for any considered intervention type. This approach has been tested for various surgeries [2,20], including DBS [15]. For some operations, such as liver surgery, the default constraints already account for the treatment's safety and efficacy by optimizing both needle trajectory and tip position. For DBS, however, the constraints we used over the electrode were mainly focused on minimizing risks (such as avoiding sulci or ventricles), and maximizing the number of contacts in the targeted structure. The objective of the present work was to improve our previous method by redefining the way the tip of the DBS electrode is placed. After numerous discussions with neurosurgeons and a careful analysis of clinical results, we have implemented a new set of constraints that optimize selection of a stimulation point location in terms of clinical outcome, within or in the vicinity of a predefined target structure chosen by the neurosurgeon.

In this paper, we present an approach covering both aspects of preoperative planning: 1) optimize the trajectory; 2) optimize the stimulation point location for a predefined target structure. For this purpose, the optimization process uses an anatomo-clinical atlas correlating clinical data with the coordinates of activated electrode contacts [22], as well as a simplified representation of the volume of tissue stimulated by the electrical signal. In this approach, the problem is solved using multi-objective optimization where the electrode trajectory and stimulation point are optimized simultaneously. One can argue that their sequential optimization (e.g., finding an optimal target location before the trajectory) may reduce the optimization complexity. However, in the previous work [18], we demonstrated that multi-objective optimization has manageable complexity and provides fast computation. In addition, choosing the target point before searching for the trajectory may, in some cases, exclude very good trajectories as a consequence. On the contrary, another stimulation point with almost similar but very slightly less optimal

quality may enable a much better trajectory and increase the overall quality of the solution.

First, we introduce the notions of anatomo-clinical atlases and volume of tissue activated used in new constraints for stimulation point selection (Sections 2.1 and 2.2, respectively). Then, in Section 2.3, we briefly describe our trajectory optimization method. Sections 2.4 and 2.5 present the stimulation point optimization methods using new constraints. Section 2.6 describes our retrospective validation study, with Section 3 presenting the results obtained. The discussion and conclusion are the last two sections.

2 Materials and Methods

2.1 Anatomo-Clinical Atlases

Neurologists use different rating scales of clinical scores to evaluate symptom severity and treatment efficacy. Each scale is dedicated to a specific symptom or aspect of quality of life. The Unified Parkinson's Disease Rating Scale (UPDRS) is the most widely used for DBS. It is divided into five parts, enabling to assess the disease's impact on several criteria: mood, speech, swallowing, dressing, and walking. The third part (UPDRS III), dedicated to motor evaluation, is the most frequently assessed. Other rating scales are also used, such as MATTIS for dementia, STROOP for cognitive functions, or the Hoehn and Yahr (H&Y) scale for symptom progress evaluation.

The concept of an *anatomo-clinical atlas* (ACA), related to clinical scores, was first proposed and fully described in 2013 by Lalys *et al.* [22]. In brief, an ACA is a predictive map that can be visualized as a normalized representation that associates stimulated points in a 3D space with patients' clinical scores for a particular rating scale, based on a retrospective study of images of patients who underwent DBS. This map can be represented as a gray-scale 3D image. Fig. 1 illustrates examples of UPDRS III atlases for the GPi. The below example was computed using the database we used in our study, detailed in Section 2.6.

For our study, an ACA for one clinical score was built using the following process. A multi-subject magnetic resonance imaging (MRI) template was created from a population of Parkinson's patients along with basal ganglia segmentation [17]. The MRIs were registered to this template using a combination of linear and non-linear registrations [21, 26]. The electrodes and their contacts were segmented from the postoperative CT images registered to the corresponding preoperative MRIs, in order to express their coordinates in the same coordinate system as for the anatomical structures. Then, for each patient, a *degree of improvement or worsening* (DIW) was defined by taking the difference between the clinical scores attributed to the patient when stimulation was ON and OFF. Since the patient's state may also deteriorate (in cases involving disease aggravation despite stimulation), the DIW can have both positive and negative values. To account for different evaluation scales, the DIW values were brought to the interval [-1,1], where -1 is the worst possible deterioration and 1 the best possible improvement, according to a given scale. The DIW of each patient was associated with a simplified estimation of the corresponding *volume of tissue activated* (VTA), *i.e.*, the part of the brain stimulated by the current (see Section 2.2). Finally, each voxel in ACA
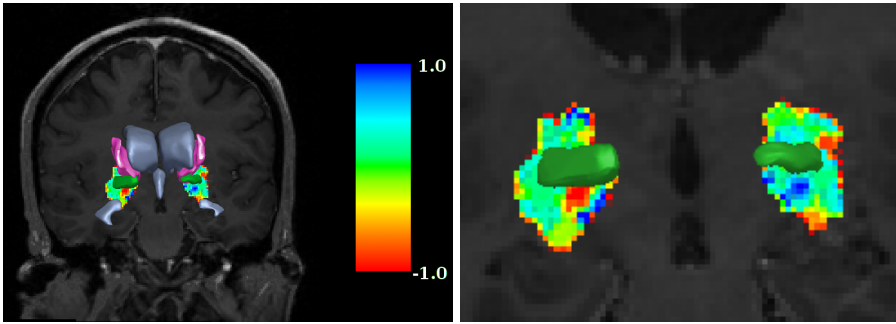
Fig. 1 Visualization example of one preoperative MRI slice, with the UPDRS III ACA for both GPi. The nuclei are represented as green 3D triangular meshes, while the ventricles and internal capsules as gray and pink meshes respectively. The computed ACA has been registered to the patient's anatomy, projected on the MRI slice, and represented as a colored map. The right figure provides a closer view at the region of interest, without the internal capsules and ventricles for a better visibility.

was associated with the average DIW corresponding to all the simplified VTAs that included this voxel. The ACA values theoretically lie within the range [-1,1]. Nevertheless, such values are actually never reached because they correspond to extreme situations that never happen. So, in practice, they are bound by the best and worst DIWs found in the set of patients used to construct the atlas. In this work, we used ACA to guide the tip of the electrode, as described in Section 2.4.

2.2 Volume of Tissue Activated

The VTA is an estimate of the volume and shape of the distribution of electrical signal stimulating brain tissues when the contact is activated. In practice, the VTA is determined by a composition of multiple settings of the electrode contacts and pulse generator, *e.g.*, the number and locations of activated contacts, impedance, voltage, pulse width, or frequency. Several research works [10–12] have proposed methods to compute and model a realistic shape of the VTA. However, one study [37] demonstrated that approximating the VTA as a spherical shape emitted from a point source is a valid simplification for monopolar stimulation. In the present study, we focused on the electrode placement algorithm instead of computing its numerical model, and used a simplified representation as a sphere with a 3 mm radius, henceforth referred to as sVTA. As the optimization algorithm we present here is completely independent from the VTA shape, it would be very easy to modify this shape, either by changing the radius of the sphere or replacing the approximation by a more complex and realistic VTA model.

The therapeutic effect depends on which brain area is stimulated. While analyzing atlases, we noted that stimulating the regions lying slightly outside of the targeted structure or on its borders (Fig. 2) can at times be prove more effective in terms of clinical outcome than stimulating only the structure's central parts. Thus, when using ACA to locate a good stimulation point, we allowed contacts to be beyond the targeted structure. Given this scenario, the stimulation may affect nearby sensitive anatomical structures. For example, in the case of GPi, an

effective target region is located close to the internal capsule (Fig. 3), which neurosurgeons tend to avoid as its stimulation may cause motor side effects [3]. Hence, that is the reason why some interventionist aim to minimize of the intersection of the sVTA with such identified anatomical structures. This issue was addressed in Section 2.5.
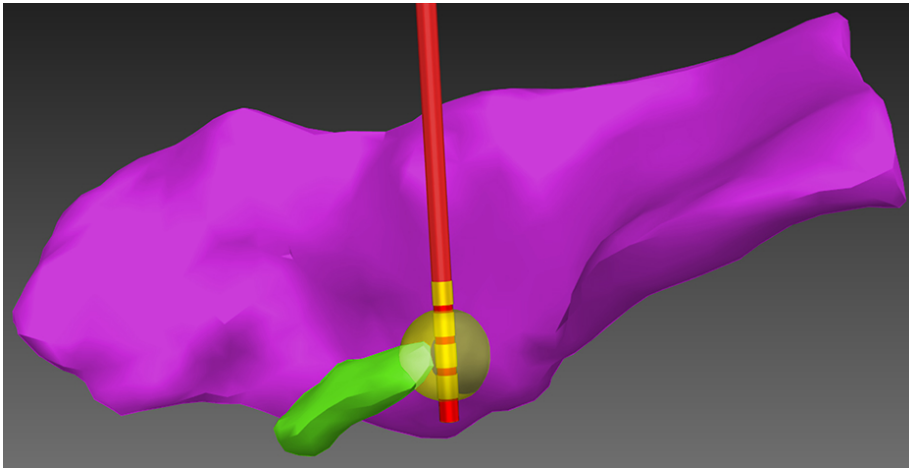

Fig. 2 Intersection of the sVTA (half transparent yellow sphere around the electrode) with the internal capsule (large pink 3D mesh in the back) while targeting the GPi (small green 3D mesh in the front) using an ACA
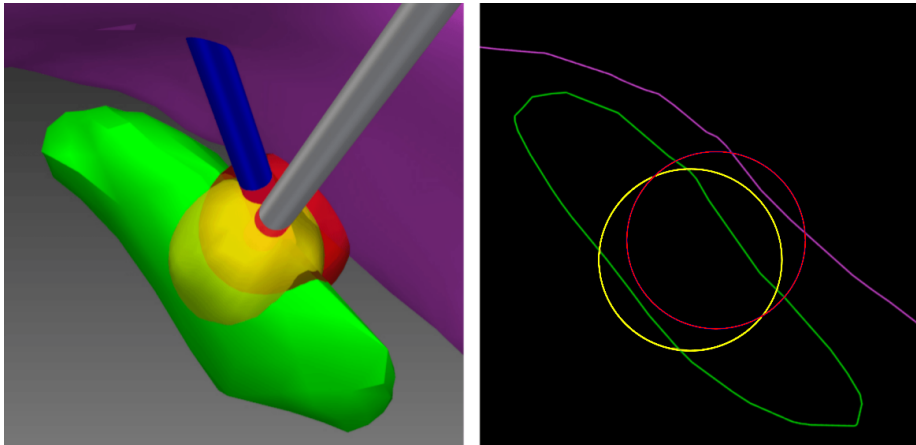

Fig. 3 Two candidate trajectories targeting the GPi (small green mesh). The trajectory (grey cylinder) that is closer to the observer is planned without using the ACA. Its sVTA (yellow sphere) is mostly centered on the targeted GPi. The farther trajectory (blue cylinder) is planned using the ACA. Its sVTA (red sphere) is shifted with a large part outside the GPi. The right image shows a section of the scene where an intersection between the sVTA of the second trajectory and the internal capsule (large pink contour) can be observed.

2.3 Optimization of the Trajectory: Global Approach

In this section, we briefly recap our previously published approach [15], on which the present method is based. It consists in fixing a set of surgical rules defined by experienced neurosurgeons for a particular intervention. The rules are transformed into geometrical constraints, formalizing them in the form of mathematical expressions. The original constraints described in [15] were based solely on anatomical considerations. In the rest of this paper, they will be referred to as *anatomical constraints*. These constraints are divided into two groups: hard constraints, *i.e.*, Boolean expressions to satisfy, and soft constraints, *i.e.*, cost functions to optimize as far as possible. An optimal trajectory is proposed after two distinct phases.

The first phase solves the hard constraints, for instance not damaging the sulci (*i.e.*, not to pass through). This phase basically consists in checking the Boolean conditions on each part of the candidate insertion surface and eliminating non-feasible parts. This enables us to define the safe insertion zone by eliminating the unfeasible candidate entry points.

The second phase solves the soft constraints (*e.g.*, maximazing the distance to the sulci). It consists in solving a multiple objective optimization problem. Each of the n soft constraints is associated with 1) a cost function $f_i(T) : \mathbb{R}^5 \to [0,1]$, where $T(x, y, z, \alpha, \beta)$ is a trajectory defined by a point $(x, y, z) \in \mathbb{R}^3$ and orientation $(\alpha, \beta) \in \mathbb{R}^2$, and 2) a weighting factor w_i reflecting the importance of this particular constraint over the others. The result of the cost function provides an estimation of trajectory T's quality with respect to the soft constraint i. A trajectory is considered optimal regarding a constraint when the value of its cost function is minimal. All cost functions are formulated in such a way as to express a constraint as a minimization problem, with results within range $[0, 1]$. The weightings were empirically defined by experienced surgeons. In this study, we made the choice to transform the multi-objective problem into a single objective problem by using a weighted sum of the cost functions. The optimum is expressed by a trajectory T_{opt} minimizing the global aggregative cost function $F : \mathbb{R}^5 \to [0, 1]$:

$$F(T) = \frac{\sum_{i=1}^n w_i \cdot f_i(T)}{\sum_{i=1}^n w_i} \tag{1}$$

Prior to optimization, an initialization with a rough estimation of trajectory samples from the first phase is performed in order to ensure good convergence [1]. Then, the optimization is performed by minimizing function $F(T)$, using the downhill simplex method introduced by Nelder and Mead [29]. Following optimization, the electrode tip is positioned at the point enabling soft constraint optimization.

One of the constraints used in the original approach described in [15] was fixed in such a way to maximize the number of electrode contacts in the target structure. As mentioned earlier, optimizations using such a constraint usually guide the tip point to inside the targeted structure. The following sections explain how we modified the process to guide the tip towards the best expected stimulation points, given that forcing the tip inside the targeted structure does not necessarily maximize the treatment's impact.

2.4 Atlas-guided Optimization of the Stimulation Point

In order to guide the planning of the tip position more accurately for the best possible outcome, we propose adding new soft constraints related to the tip position for the optimization process. These new constraints are optimized along with the initial anatomical constraints. The maximization of the number of electrode contacts inside the predefined targeted structures is no longer used, but replaced by the information from ACA, as described below.

First, we define the function returning the value of the atlas $\mathcal{A}_s$ of clinical score s at a specific voxel as $ACA : \mathbb{R}^3 \to [-1, 1]$. Representing the atlas values in the range [-1,1] allows a more intuitive reading and understanding of the atlas by surgeons. However, in the automatic optimization process, for a fair comparison with all other anatomical constraints, it is necessary to normalize the $\mathcal{A}_s$ values within the same specific range of $[0, 1]$. We define the *normalized anatomo-clinical atlas* (N-ACA) using equation 2.

$$N\text{-}ACA(\mathcal{A}_S, p(T)) = \frac{ACA_{max} - ACA(\mathcal{A}_s, p(T))}{ACA_{max} - ACA_{min}} = \frac{1 - ACA(\mathcal{A}_s, p(T))}{2}, \quad (2)$$

where $ACA(\mathcal{A}_s, p(T))$ is the value corresponding to the atlas $\mathcal{A}_s$ at the voxel located at the contact point $p(T)$ of the considered candidate trajectory T; ACA_{min} and ACA_{max} correspond to the theoretically possible maximal and minimal values of any ACA: -1 and 1.

To guide the tip towards the best location of a single atlas, we define a new cost function using the N-ACA. For a clinical score s, the corresponding normalized cost function $f_{\mathcal{A}_S} : \mathbb{R}^5 \to [0, 1]$ simply returns the value of the N-ACA at the location of the active contact point $p(T) : f_{\mathcal{A}_S}(T) = N\text{-}ACA(\mathcal{A}_s, p(T))$.

Using the new cost function $f_{\mathcal{A}_S}(T)$ in equation (1), the global cost function $F(T)$ to minimize becomes:

$$F(T) = \frac{\left(\sum_{i=1}^{n} w_i \cdot f_i(T)\right) + w_{\mathcal{A}_S} \cdot f_{\mathcal{A}_S}(T)}{\left(\sum_{i=1}^{n} w_i\right) + w_{\mathcal{A}_S}} \quad (3)$$

where $f_i(T)$ and w_i are the cost function and the weighting factor of each anatomical soft constraint i, n is the number of anatomical soft constraints, and $f_{\mathcal{A}_S}(T)$ and $w_{\mathcal{A}_S}$ are respectively the normalized cost function and weighting factor chosen by the neurosurgeon, corresponding to the atlas of clinical score s.

2.5 VTA-guided Optimization of the Stimulation Point

When using the ACA constraint, the tip can be guided to outside the targeted structure. An active contact point placed in such a location may stimulate nearby structures and cause potential side effects. In the second part of our work, we focused our attention on avoiding stimulating nearby structures. We introduce another type of constraint based on the computed intersection between the sVTA and a 3D mesh.

One suitable constraint is added for each nearby structure to avoid its stimulation. The constraint can express that the structure needs to be completely or

only partially avoided, with a defined maximum intersection. As for other soft constraints, each inspected trajectory is penalized in proportion to how much it violates of the constraint. If the constraint is respected, the trajectory is not discriminated by the solver.

The new *intersection volume* (IV) soft constraint states that for any trajectory T, the intersection volume $\mathcal{I}_s(T)$ between its sVTA and the structure s to avoid should be less than or equal to $x_s\%$ of the total sVTA volume. When $x_s = 0$, the structure is avoided completely. The mathematical expression of the associated cost function $f_{\mathcal{I}_s}$ is written as:

$$f_{\mathcal{I}_s}(T) = max\left(\frac{\mathcal{I}_s(T) - x_s}{100 - x_s}, 0\right) \qquad (4)$$

Equation 4 enables a normalized representation of the IV constraint: the result of $f_{\mathcal{I}_s}$ ranges from 0 when $\mathcal{I}_s(T) < x_s\%$ to 1 when $\mathcal{I}_s(T)$ is 100% of the sVTA. This constraint can be included in the global cost function as follows:

$$F(T) = \frac{\left(\sum_{i=1}^{n} w_i \cdot f_i(T)\right) + w_{\mathcal{A}_R} \cdot f_{\mathcal{A}_R}(T) + w_{\mathcal{I}_s} \cdot f_{\mathcal{I}_s}(T)}{\left(\sum_{i=1}^{n} w_i\right) + w_{\mathcal{A}_R} + w_{\mathcal{I}_s}} \qquad (5)$$

where $w_{\mathcal{I}_s}$ is the weight given to the IV constraint for structure to avoid s.

2.6 Input Data and Experiments

To validate our method, we conducted a retrospective study on a dataset of Parkinson's disease patients from the University Hospital Rennes Pontchaillou (Rennes, France). The cases were randomly selected from a subset of patients who underwent stimulation of the GPi. The goal of this study was to analyze the influence of two types of information on the results of the preoperative planning process: anatomo-clinical atlas and intersection of the sVTA with other structures. Only one clinical score, UPDRS III, was used in this study, in order to avoid bias in validation due to the mutual influence of scores. Its ACA will be referred to as $\mathcal{A}_{\mathrm{UP}}$. The minimization of the intersection between the sVTA and internal capsule was investigated. The intersection will be referred to as $\mathcal{I}_{\mathrm{IC}}$. Our surgeons defined the maximal tolerance of x_{IC} as equal to 20% of the sVTA volume lying within the internal capsule.

The validation process consisted in comparing trajectories obtained by different types of planning between them. We considered three types of planning for comparison:

P1: planning with anatomical constraints only, as proposed by the previous method described in Section 2.3,
P2: planning with anatomical constraints + ACA constraint,
P3: planning with anatomical constraints + ACA constraint + IV constraint.

For all three types of planning, the anatomical constraints to minimize were those previously described in more detail in [14]:

- "ST": orientation of the electrode, computed as the proximity to the standard trajectory defined by expert neurosurgeons and commonly used in the commercial platforms.
- "DS": distance from the electrode to the the closest sulcus.
- "DV": distance from the electrode to the ventricles.

Cost function f_{ST} associated to soft constraint ST was defined as equation (6), where T is a candidate trajectory and T_S is the standard trajectory:

$$f_{ST} = \frac{angle(T, T_S)}{90} \qquad (6)$$

The associated cost functions of DS and DV constraints were built on the model of equation (7), where T is a candidate trajectory, AS the anatomical structure to avoid (sulci or ventricles), D_{minAS} the distance at which the trajectory is considered safe regarding structure AS:

$$f_{D_{AS}} = max\left(\frac{D_{minAS} - dist(T, AS)}{D_{minAS}}, 0\right) \qquad (7)$$

These cost functions have been formulated so that they can express the constraint as a minimization problem, and their result is within the range [0,1].

Their associated weighting factors were set to the typical default values chosen by our neurosurgeon: $w_{ST} = 0.2$, $w_{DS} = 0.4$ and $w_{DV} = 0.4$ for ST, DS and DV constraints, respectively. Note that this setting can be modified in the GUI and the result is updated instantaneously.

For the new ACA and IV constraints, we tried different settings of weighting factors to analyze their impact. For planning type P2 (described above), the weightings $w^1_{\mathcal{A}_{UP}} = 0.1$, $w^2_{\mathcal{A}_{UP}} = 0.5$ and $w^3_{\mathcal{A}_{UP}} = 0.9$ were alternatively assigned to the ACA constraint. For the planning type P3, when testing both the atlas and intersection volume constraints, we also assigned the same three weight values to the IV constraint. Thus, we tested nine different weighting combinations of $W_{m,n}$ that represent the use of $w^m_{\mathcal{A}_{UP}}$ and $w^n_{\mathcal{I}_{IC}}$, as listed in Table 1.

We denote T_{imp} as the trajectory of the implanted electrode and T_{P1}, T_{P2}, and T_{P3} as the optimal trajectories produced with plannings P1, P2, and P3, respectively. We defined the following comparison criteria:

C1: comparison of the ACA values between computed trajectories T_{P1}, T_{P2}, and T_{P3}

C2: comparison of the intersection volumes $\mathcal{I}_{IC}(T_{P1})$, $\mathcal{I}_{IC}(T_{P2})$, and $\mathcal{I}_{IC}(T_{P3})$ in terms of percentage of the sVTA volume covering internal capsule,

C3: comparison of the minimal distances from the trajectories to the ventricles and sulci, representing trajectory risk degree.

For this study, we disposed of a dataset of nine patients undergone bilateral stimulation, resulting in 18 test cases. Each patient underwent 3T T1-weighted MRI and CT scans just before the intervention, then postoperative CT scans a few days after. The preprocessing of the images was performed using the pyDBS pipeline described in [13], successively involving denoising, bias correction on MRI, CT image registration to preoperative MRI, automatic segmentation and 3D mesh reconstructions. In the same coordinate system, we obtained 3D triangular meshes of all structures of interest in the brain (including the GPi, ventricles, sulci, skin,

Table 1 Tested weighting combinations

Combination #	Combination notation	Weight $w^*_{\mathcal{A}_{\mathrm{UP}}}$ of ACA constraint	Weight $w^*_{\mathcal{I}_{\mathrm{IC}}}$ of IV constraint
1	$W_{1,1}$	0.1	0.1
2	$W_{1,2}$	0.1	0.5
3	$W_{1,3}$	0.1	0.9
4	$W_{2,1}$	0.5	0.1
5	$W_{2,2}$	0.5	0.5
6	$W_{2,3}$	0.5	0.9
7	$W_{3,1}$	0.9	0.1
8	$W_{3,2}$	0.9	0.5
9	$W_{3,3}$	0.9	0.9

and internal capsule), as well as implanted electrodes (segmented from postoperative CTs) and locations of active contact points. Note that in the absence of angiography, we used the sulci mesh to avoid vessels, as often performed in clinical routine. In addition, we used UPDRS III scores acquired 3 months prior to surgery (Dopa OFF) and 6 months after (stimulation ON, Dopa OFF) in order to compute a DIW for each patient.

We applied a leave-one-out cross-validation approach, computing an UPDRS III atlas for each patient using the DIW of all other patients. The worst DIW was equal to -0.115, and the best to 0.543, within the maximum range of [-1,1]. The ACA was then registered to the preoperative MRIs using nonrigid registration. We computed optimal trajectories for planning types P1, P2 and P3, and then measured their value in the ACA (representing the expected DIW), intersection volumes, and distances to critical structures.

3 Results

The results of our retrospective study are summarized in Tables 2, 3, 4, and 5. Table 2 presents the comparison according to criterion C1. ACA values for the trajectories obtained using two different planning methods are shown: 1) the original planning method P1, and 2) the new planning method P2 using the ACA constraint with different weighting factors P2-$w^1_{\mathcal{A}_{\mathrm{UP}}}$, P2-$w^2_{\mathcal{A}_{\mathrm{UP}}}$, P2-$w^3_{\mathcal{A}_{\mathrm{UP}}}$. In this table, the DIW obtained from the actual UPDRS III scores ON/OFF of each patient when stimulating using the implanted electrode T_{imp} is provided for information. Table 2 also displays an equivalence of the actual and expected average improvements in the UPDRS III scale for the implanted electrodes and planned trajectories, respectively. Contrary to DIW, an improvement in UPDRS scale signifies a decrease in score, thus explaining the negative values in the table.

A two-tailed Student's t-test was used to test the statistical significance between the DIW of trajectories pairwise with the null hypothesis that the methods return identical values. In all cases, the electrode placement proposed by the new planning P2 obtained higher scores than P1 which used anatomical constraints only. These results were statistically significant for the three versions of P2, p-values of 0.00592 for P2-$w^1_{\mathcal{A}_{\mathrm{UP}}}$, 0.00028 for P2-$w^2_{\mathcal{A}_{\mathrm{UP}}}$, and 0.00025 for P2-$w^3_{\mathcal{A}_{\mathrm{UP}}}$, all of which notable being under the threshold of 0.01.

Table 3 summarizes the average values and standard deviations of all DIW corresponding to computed trajectories for each of the nine weighting combinations

Table 2 Actual DIW for the implanted electrodes T_{imp}, expected DIW extracted from ACA values for the trajectories proposed by plannings $P1$, P2-$w^1_{\mathcal{A}_{\mathrm{UP}}}$, P2-$w^2_{\mathcal{A}_{\mathrm{UP}}}$ and P2-$w^3_{\mathcal{A}_{\mathrm{UP}}}$, and equivalence of the average improvement and its standard deviation in the UPDRS III scores

Case	Implented	P1	P2		
#	T_{imp}	T_{P1}	$T_{P2\text{-}w^1_{\mathcal{A}_{\mathrm{UP}}}}$	$T_{P2\text{-}w^2_{\mathcal{A}_{\mathrm{UP}}}}$	$T_{P2\text{-}w^3_{\mathcal{A}_{\mathrm{UP}}}}$
			values in DIW/ACA scale		
1	-0.101	0.188	0.188	0.233	0.233
2	-0.101	0.193	0.199	0.199	0.199
3	-0.086	0.179	0.350	0.350	0.252
4	-0.086	0.140	0.196	0.243	0.226
5	0.343	0.064	0.187	0.354	0.354
6	0.343	0.174	0.174	0.183	0.183
7	-0.115	0.176	0.291	0.291	0.291
8	-0.115	0.146	0.174	0.193	0.193
9	0.343	-0.115	0.405	0.405	0.405
10	0.343	0.123	0.286	0.180	0.180
11	0.200	0.176	0.212	0.233	0.350
12	0.200	0.150	0.343	0.343	0.343
13	0.086	0.204	0.204	0.405	0.405
14	0.086	0.185	0.187	0.343	0.343
15	0.543	0.176	0.343	0.336	0.343
16	0.543	0.139	0.155	0.166	0.174
17	0.157	0.106	0.133	0.254	0.254
18	0.157	0.140	0.204	0.221	0.221
AVG	0.152	0.141	0.235	0.274	0.275
STD	0.223	0.073	0.080	0.080	0.080
			equiv. in UPDRS III scale		
AVG	-10.7	-9.9	-16.5	-19.2	-19.2
STD	15.6	5.1	5.6	5.6	5.6

Table 3 Average DIW and standard deviations for trajectories proposed by planning P3 using nine different weighting combinations $W_{m,n}$ for ACA and IV constraints.

	$W_{1,1}$	$W_{1,2}$	$W_{1,3}$	$W_{2,1}$	$W_{2,2}$	$W_{2,3}$	$W_{3,1}$	$W_{3,2}$	$W_{3,3}$
AVG	0.219	0.214	0.214	0.265	0.240	0.238	0.262	0.252	0.242
STD	0.068	0.061	0.061	0.074	0.057	0.059	0.070	0.061	0.057

of planning type P3. We can see that, on average, P3 also provided better scores than P1 (all p-values < 0.01).

When analyzing the results of the comparison with criterion C2, we first observed that the sVTA of three implanted electrodes (cases 1, 5 and 10) partially entered the internal capsule, with $\mathcal{I}_{\mathrm{IC}}(T_{imp1}) = 5.83\%$, $\mathcal{I}_{\mathrm{IC}}(T_{imp5}) = 12.44\%$ and $\mathcal{I}_{\mathrm{IC}}(T_{imp10}) = 5.59\%$, respectively. All were under the fixed threshold $x_{IC} = 20\%$. Planning type P1 produced no intersection. Planning P2 (using the ACA constraint) increased their frequency, as expected. Such intersections were observed in 12 of all 18 cases for at least one of the tested weighting factors (see Table 4, columns P2). Of these, six intersections with $\mathcal{I}_{\mathrm{IC}}(T_{P2}) > 20\%$ were detected, one even approaching to 100% (highlighted in bold). This emphasizes the necessity

Table 4 Intersection volume $\mathcal{I}_{\mathrm{IC}}$ (in %) for trajectories produced by planning types P2 and P3 with different weighting settings for the ACA and IV constraints. Extensive intersections with $\mathcal{I}_{\mathrm{IC}} > 20\%$ are in bold. Average values are calculated including all 18 cases, but only the cases producing at least one intersection are displayed

| Case | low weight for atlas | | | | medium weight for atlas | | | | high weight for atlas | | | |
| | P2 | P3 | | | P2 | P3 | | | P2 | P3 | | |
#	$T_{P2\text{-}w^1_{A_{\mathrm{UP}}}}$	$T_{P3\text{-}W_{1,1}}$	$T_{P3\text{-}W_{1,2}}$	$T_{P3\text{-}W_{1,3}}$	$T_{P2\text{-}w^2_{A_{\mathrm{UP}}}}$	$T_{P3\text{-}W_{2,1}}$	$T_{P3\text{-}W_{2,2}}$	$T_{P3\text{-}W_{2,3}}$	$T_{P2\text{-}w^3_{A_{\mathrm{UP}}}}$	$T_{P3\text{-}W_{3,1}}$	$T_{P3\text{-}W_{3,2}}$	$T_{P3\text{-}W_{3,3}}$
3	9.39	5.86	-	-	15.15	15.15	-	-	-	-	-	-
4	-	-	-	-	**26.38**	**26.38**	-	-	**38.70**	**38.70**	15.90	-
5	-	-	-	-	7.59	7.59	-	-	15.68	7.07	7.07	0.13
7	7.52	7.52	3.60	3.60	3.35	3.35	3.35	3.35	6.49	4.87	4.87	4.49
8	-	-	-	-	2.17	1.09	1.09	1.09	2.86	2.86	2.86	2.86
9	13.81	-	-	-	8.16	-	-	-	6.65	-	-	-
10	**96.58**	-	-	-	-	-	-	-	-	-	-	-
12	0.80	0.80	-	-	-	-	-	-	**33.60**	5.38	-	-
13	-	-	-	-	**59.65**	**35.50**	3.13	-	**37.68**	**37.68**	18.62	6.53
15	15.65	7.90	5.33	5.33	10.86	10.20	7.32	-	9.56	-	-	-
16	7.55	-	-	-	0.71	-	-	-	-	-	-	-
17	0.01	-	-	-	-	-	-	-	-	-	-	-
AVG	8.41	1.23	0.50	0.50	7.45	5.51	0.83	0.27	8.40	5.36	2.74	0.78

Table 5 Average minimal distances to the sulci and ventricles for the implanted trajectories T_{imp} and trajectories proposed by the planning types $P1$ and P3-$W_{2,3}$

	Min. distance to sulci (mm)			Min. distance to ventricles (mm)		
	T_{imp}	T_{P1}	$T_{P3\text{-}W_{2,3}}$	T_{imp}	T_{P1}	$T_{P3\text{-}W_{2,3}}$
AVG	2.451	8.712	8.952	7.950	11.603	11.852
STD	1.397	2.132	2.287	2.212	1.531	1.352

of adding a restricting constraint minimizing the intersection between the sVTA and internal capsule. Table 4 also shows the intersection volume $\mathcal{I}_{\mathrm{IC}}$ for all experimented weightings of P3. We can first notice that higher values for the weighting factor of the atlas (rightmost block) led to a higher number of intersections, which were particularly extensive. Secondly, we observe a decrease of the overall number of intersections using P3 compared to P2.

The most advantageous weighting combination for planning P3 would increase the DIW and decrease the $\mathcal{I}_{\mathrm{IC}}$. Thus, we measured a ratio R between the average DIW and $\mathcal{I}_{\mathrm{IC}}$ for each combination so as to determine the best one. Fig.4 illustrates the R values for each weighting combination $W_{m,n}$. A large gap can clearly be observed between $W_{2,3}$ and the other settings. This analysis led us to state that a probable reasonable choice would be close to the combination $w^2_{\mathcal{A}_{\mathrm{UP}}} = 0.5$ and $w^3_{\mathcal{I}_{\mathrm{IC}}} = 0.9$, thus enabling maximally-reduced intersections while preserving good DIW. However, this first study has only considered a small set of representative weights with a low, medium and high values. Further analysis would be required to recommend appropriate weights with more accuracy.

To confirm that our new planning approach does not reduce safety, we present the minimal distances to the sulci and ventricles for trajectories T_{imp}, T_{P1}, and $T_{P3\text{-}W_{2,3}}$ in Table 5. We can observe that the average minimal distances for $P1$ and P3-$W_{2,3}$ were relatively similar (p-values > 0.05 demonstrating that there was no statistically significant difference), with even higher values than for T_{imp}. This shows that our new approach increases the chances of improving outcomes while preserving safety by providing a higher DIW than with the previous approach, yet avoiding the surrounding sensitive structures. An example of the results of different planning types can be found in Fig.5.

All experiments were performed on a computer equipped with an intel Core i5 processor at 2.67GHz, 12GB RAM, and a NVIDIA GeForce GTX 275 graphics card. For each case, the overall planning process took less than 3 seconds for P1 and P2, and less than 10 seconds for P3. The code for computing new target-based constraints was executed on CPU only, with no optimization, thus enabling further acceleration.

4 Discussion

Due to our new approach, we are able to automatically compute safe and optimal electrode placements, improving expected treatment efficacy by taking into account previous outcomes. Anatomo-clinical atlases help inform and boost the decision-making process for choosing the best stimulation point in an effort to
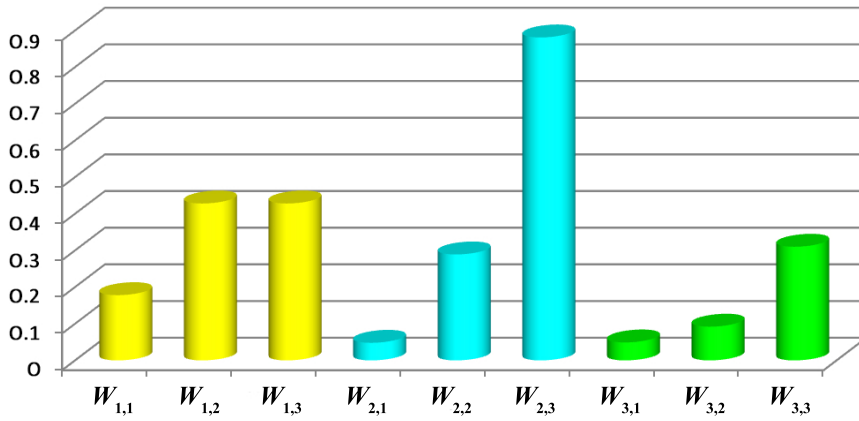
Fig. 4 Ratio R illustrating the benefits of each weighting combination for planning type P3
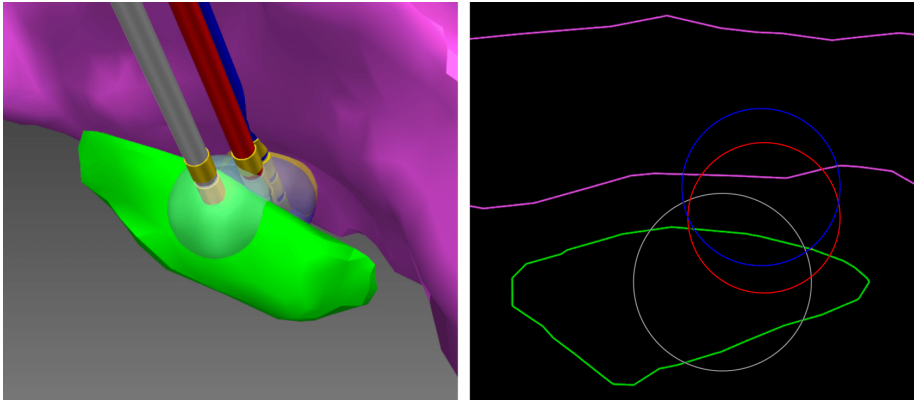

Fig. 5 Results of different planning types for the same patient: P1 (left electrode and sVTA), P2 (right electrode and sVTA), and P3 (middle electrode and sVTA). We can observe no intersection with the internal capsule for P1, a large intersection for P2, and a relatively small intersection for P3.

maximize benefits, while computing the intersection between the sVTA and internal capsule helps minimize side effects.

In practice, the atlas values lay within the interval [-0.155; 0.543], bound by the best and the worst DIW of the patients used to build the atlases. For cases #15 and #16, when the patient had the highest DIW of 0.543 for T_{imp}, our software could not propose a trajectory with a similar DIW, as using the leave-one-out approach meant the atlas was constructed without this patient. This means that, in this particular case, the maximal DIW was 0.343, the second best of all values. This value was the highest we could expect from the solver. If there had been any greater DIW in the atlas, our solver would potentially have proposed a better solution for this case. An atlas built with more cases would, evidently, lead to a better sampling of the solution space.

The IV constraint was designed so that only an intersection greater than 20% would be detected by the solver. This means it should not detect a difference between two small intersections, yet in Table 4 we can observe that we minimized the $\mathcal{I}_{IC}$ even for small intersections by increasing the weighing factor for the IV constraint. This phenomenon is associated with the optimization algorithm we used. The increase in $w_{\mathcal{I}_{IC}}$ moved the electrode tip away from the internal capsule by pushing the solver to explore more solutions with small intersections during the execution of the optimization algorithm.

The shape used in this study to represent the VTA was not exact or simulated, but approximated by a 3-mm radius sphere, as this study focused on the placement algorithm. However, the approach we proposed is generic and applicable to any kind of VTA shape when computing the intersection volume. As a matter of fact, the VTA shape changes in time together with the conductivity of a patient's brain tissues. In our software, it is possible to replace the sphere mesh either by a computed model [9] or a sphere of variable radius, which can be determined interactively or by a constraint designed to maximize the benefits and lower the risks according to the placement. Moreover, the proposed technique is generic enough to be easily used when multiple contacts are activated on the electrode, by using an aggregation of meshes to represent the VTA and compute the intersection volume.

Our software offers the opportunity to interactively adjust the weighting factors of the constraints. As with most tools offering computerized assistance in the decision-making process, it aims to help the surgeon make decisions, providing as much information as possible and suggesting solutions, without imposing settings or results. This is the reason why we proposed some default values in this study for the weighting factors, though these can be adjusted in real time during the planning according to each patient's needs and specificities. To propose the default values, we tried three sample weightings for each constraint. While further studies will be needed to define the most appropriate values more accurately, we believe that this can already provide a good starting point for surgeons. We also proposed in [18] an alternative optimization approach based on Pareto front that does not require the definition of weightings for each constraint in order to obtain one particular trajectory, proposing rather a whole set of optimal solutions. Another option to help the surgeon calibrate the tool is to perform a statistical study in order to learn the most appropriate parameters on past cases, and set them as default, as we previously proposed in [14].

If the patient suffers from multiple symptoms of different types, the surgeon may want to consider multiple atlases for defining the stimulation point. Moreover, all the considered clinical scores may hold different significance in the decision. The definition of the constraints depends on neurosurgeon's choice and patient's situation, usually being a trade-off between benefits and losses and highly patient-specific. Here, we face a multi-objective problem as well, with different weightings that need to be adjusted by the neurosurgeon. Although not detailed in the paper, our software proposes the possibility of combining atlases. The resulting multi-atlas is computed as the weighted sum of all individual N-ACAs. A further study would allow for investigation of this functionality relevance and appropriate validation.

With the use of an anatomo-clinical atlas, our software can also serve as a simulation tool to have a rough estimation of the expected outcome for the patient in relation to a clinical score. However, for now an ACA should not be seen as a

mathematical formula that can give an accurate prediction of an outcome for a specific stimulation point, but rather as a map that correlates stimulation locations with a trend towards improvement or worsening of a clinical score. Thus, our algorithm proposes to automatically guide the target point towards locations with most promising trend. Yet, a separate study has to be conducted to prove correctness of the constructed ACA. The quality of the brain structures segmentation and atlas-to-patient registration may also affect the ACA accuracy and optimization results. For instance, GPi is known to have lower contrasts on T1w MRI complicating its correct segmentation. However, as shown in [17], the registration method used in this work provides satisfactory results with strong Dice-Kappa coefficients from 0.64 to 0.86 for different brain structures. Since effective stimulation locations represent nucleus regions rather than isolated points, this registration accuracy is sufficient for bringing the optimizer in the desired area. As the ACA score is only one of the optimization objectives, a better registration would not significantly change the optimization results.

One limitation to the use of such atlases is that they represent an average across a population, and do not take into account the various phenotypes of patients. In future works, using separate atlases for different clusters of population could be considered to avoid this bias.

5 Conclusion

We presented the first automatic optimization approach for the preoperative planning of DBS electrode trajectories that simultaneously optimizes the target point location and electrode trajectory. Extending our previous approach optimizing electrode trajectory, we imposed two additional constraints over the tip of the electrode, helping to more accurately define its location. The first was based on anatomo-clinical atlases and used to improve the outcome of the operation and have a more positive impact to the patient's state, based on the study of previous cases. The second minimized the influence of the electric signal on surrounding anatomical structures to reduce possible side effects. Compared to our previous approach, this retrospective study confirmed that our new method proposed solutions with higher scores and minimal signal intersections with the internal capsule, while keeping the trajectory at a safe distance from critical structures.

References

1. Baegert, C., Essert-Villard, C., Schreck, P., Soler, L., Gangi, A.: Trajectory optimization for the planning of percutaneous radiofrequency ablation of hepatic tumors. Computer Aided Surgery **12**(2), 82–90 (2007)
2. Baegert, C., Villard, C., Schreck, P., Soler, L.: Multi-criteria trajectory planning for hepatic radiofrequency ablation. In: proceedings of MICCAI'07, vol. 4791, pp. 584–592. Springer LNCS (2007)
3. Baker, K.B., Boulis, N.M., Rezai, A.R., Montgomery Jr, E.B.: Target selection using microelectrode recording. In: Z. Israel, K.J. Burchiel (eds.) Microelectrode Recordings in Movement Disorder Surgery, pp. 138–151. Thieme New York (2004)
4. Bériault, S., Drouin, S., Sadikot, A.F., Xiao, Y., Collins, D.L., Pike, G.B.: A prospective evaluation of computer-assisted deep brain stimulation trajectory planning. In: In proceedings of CLIP'12, vol. 7761, pp. 42–49. Springer LNCS (2013)
5. Bériault, S., Subaie, F., Mok, K., Sadikot, A., Pike, G.B.: Automatic trajectory planning of DBS neurosurgery from multi-modal MRI datasets. In: proceedings of MICCAI'11, vol. 6891, pp. 259–266. Springer LNCS (2011)
6. Bériault, S., Xiao, Y., Bailey, L., Collins, D., Sadikot, A., Pike, G.: Towards computer-assisted deep brain stimulation targeting with multiple active contacts. In: In proceedings of MICCAI'12, vol. 7510, pp. 487–494. Springer LNCS (2012)
7. Bourbakis, N., Awad, M.: A 3-D visualization method for image-guided brain surgery. IEEE Transactions on Systems, Man, and Cybernetics, Part B: Cybernetics **33**(5), 766–781 (2003)
8. Brunenberg, E., Vilanova, A., Visser-Vandewalle, V., Temel, Y., Ackermans, L., Platel, B., ter Haar Romeny, B.: Automatic trajectory planning for deep brain stimulation: A feasibility study. In: proceedings of MICCAI'07, vol. 4791, pp. 584–592. Springer LNCS (2007)
9. Butson, C., Cooper, S., Henderson, J., McIntyre, C.: Patient-specific analysis of the volume of tissue activated during deep brain stimulation. NeuroImage **34**, 661–670 (2007)
10. Butson, C.R., McIntyre, C.C.: Role of electrode design on the volume of tissue activated during deep brain stimulation. Journal of Neural Engineering **3**(1), 1 (2005)
11. Chaturvedi, A., Butson, C.R., Lempka, S.F., Cooper, S.E., McIntyre, C.C.: Patient-specific models of deep brain stimulation: Influence of field model complexity on neural activation predictions. Brain Stimulation **3**(2), 65–77 (2010)
12. Chaturvedi, A., Luján, J., McIntyre, C.: Artificial neural network based characterization of the volume of tissue activated during deep brain stimulation. J. Neural Eng. **10**(5), 056,023 (2013)
13. D'Albis, T., Haegelen, C., Essert, C., Fernandez-Vidal, S., Lalys, F., Jannin, P.: Pydbs: an automated image processing workflow for deep brain stimulation surgery. International journal of computer assisted radiology and surgery pp. 1–12 (2014)
14. Essert, C., Fernandez-Vidal, S., Capobianco, A., Haegelen, C., Karachi, C., Bardinet, E., Marchal, M., Jannin, P.: Statistical study of parameters for deep brain stimulation automatic preoperative planning of electrodes trajectories. International Journal of Computer Assisted Radiology and Surgery pp. 1–11 (2015). DOI 10.1007/s11548-015-1263-5
15. Essert, C., Haegelen, C., Lalys, F., Abadie, A., Jannin, P.: Automatic computation of electrodes trajectories for deep brain stimulation: A hybrid symbolic and numerical approach. Int. Journal of Computer Assisted Radiology and Surgery **7**(4), 517–532 (2012)
16. Fujii, T., Emoto, H., Sugou, N., Mito, T., Shibata, I.: Neuropath planner-automatic path searching for neurosurgery. In: proceedings of CARS'03, vol. 1256, pp. 587–596. Elsevier (2003)
17. Haegelen, C., Coupé, P., Fonov, V., Guizard, N., Jannin, P., Morandi, X., Collins, D.L.: Automated segmentation of basal ganglia and deep brain structures in mri of parkinson's disease. Int. J. Comput. Assist. Radiol. Surg. **8**(1), 99–110 (2013)
18. Hamze, N., Voirin, J., Collet, P., Jannin, P., Haegelen, C., Essert, C.: Pareto front vs. weighted sum for automatic trajectory planning of deep brain stimulation. In: Medical Image Computing and Computer Assisted Intervention (MICCAI'16), *LNCS*, vol. 9900, pp. 534–541. Springer (2016)
19. Herzog, J., Fietzek, U., Hamel, W., Morsnowski, A., Steigerwald, F., Schrader, B., Weinert, D., Pfister, G., Muller, D., Mehdorn, H., Deuschl, G., Volkmann, J.: Most effective stimulation site in subthalamic deep brain stimulation for parkinson's disease. Movement Disorders **19**(9), 1050 –1099 (2004)

20. Jaberzadeh, A., Essert, C.: Multi-probe three-dimensional placement planning for liver cryosurgery: comparison of different optimization methods. In: proceedings of CMMSE'14, vol. 3, pp. 743–754 (2014)
21. Lalys, F., Haegelen, C., Abadie, A., Jannin, P.: Post-operative assessment in Deep Brain Stimulation based on multimodal images: registration workflow and validation. In: proceedings of SPIE Medical Imaging, vol. 7261(1), p. 72612M (2009)
22. Lalys, F., Haegelen, C., Maroua, M., Drapier, S., Verin, M., Jannin, P.: Anatomo-clinical atlases correlate clinical data and electrode contact coordinates: application to subthalamic deep brain stimulation. Journal of Neuroscience Methods **212**(2), 297–307 (2013)
23. Lee, J., Huang, C., Lee, S.: Improving stereotactic surgery using 3-D reconstruction. IEEE Engineering in Medicine and Biology Magazine **21**(6), 109–116 (2002)
24. Liu, Y., Konrad, P., Neimat, J., Tatter, S., Yu, H., Datteri, R., Landman, B., Noble, J., Pallavaram, S., Dawant, B., D'Haese, P.F.: Multisurgeon, multisite validation of a trajectory planning algorithm for deep brain stimulation procedures. IEEE Transactions on Biomedical Engineering **61**(9), 2479–2487 (2014)
25. Maks, C., Butson, C., Walter, B., Vitek, J., C.C., M.: Deep brain stimulation activation volumes and their association with neurophysiological mapping and therapeutic outcomes. J. Neurol. Neurosurg. Psychiatry **80**, 659–666 (2009)
26. Mehri, M., Lalys, F., Maumet, C., Haegelen, C., Jannin, P.: Analysis of electrodes' placement and deformation in deep brain stimulation from medical images. In: proceedings of SPIE Medical Imaging, vol. 8316(1), p. 831632 (2012)
27. Mikos, A., Bowers, D., Noecker, A., McIntyre, C., Won, M., Chaturvedi, A., Foote, K., Okun, M.: Patient-specific analysis of the relationship between the volume of tissue activated during dbs and verbal fluency. Neuroimage **54S1**, 238–246 (2011)
28. Navkar, N., Tsekos, N., Stafford, J., Weinberg, J., Deng, Z.: Visualization and planning of neurosurgical interventions with straight access. In: proceedings of IPCAI'10, vol. 6135, pp. 1–11. Springer LNCS (2010)
29. Nelder, J., Mead, R.: A simplex method for function minimization. Computer Journal **7**(4), 308–313 (1965). DOI 10.1093/comjnl/7.4.308
30. Nowinski, W., Yang, G., Yeo, T.: Computer-aided stereotactic functional neurosurgery enhanced by the use of the multiple brain atlas database. IEEE Transactions on Medical Imaging **19**(1), 62–69 (2002)
31. Pallavaram, S., D'Haese, P.F., Lake, W., Konrad, P.E., Dawant, B.M., Neimat, J.S.: Fully automated targeting using non-rigid image registration matches accuracy and exceeds precision of best manual approaches to subthalamic deep brain stimulation targeting in parkinson's disease. Neurosurgery **76**(6), 756–765 (2015)
32. Saint-Cyr, J., Hoque, T., Pereira, L., Dostrovsky, J., Hutchison, W., Mikulis, D., Abosch, A., Sime, E., Lang, A., Lozano, A.: Localization of clinically effective stimulating electrodes in the human subthalamic nucleus on magnetic resonance imaging. J. Neurosurg. **97**, 1152–1166 (2002)
33. Shamir, R., Tamir, I., Dabool, E., Joskowicz, L., Shoshan, Y.: A method for planning safe trajectories in image-guided keyhole neurosurgery. In: proceedings of MICCAI'10, vol. 6363, pp. 457–464. Springer LNCS (2010)
34. Tirelli, P., de Momi, E., Borghese, N., Ferrigno, G.: An intelligent atlas-based planning system for keyhole neurosurgery. In: Computer Assisted Radiology and Surgery supplemental, pp. S85–S91 (2009)
35. Tisch, S., Zrinzo, L., Limousin, P., Bhatia, K., Quinn, N., Ashkan, K., Hariz, M.: Effect of electrode contact location on clinical efficacy of pallidal deep brain stimulation in primary generalised dystonia. J. Neurol. Neurosurg. Psychiatry **78**, 1314–1319 (2007)
36. Vaillant, M., Davatzikos, C., Taylor, R., Bryan, R.: A path-planning algorithm for image-guided neurosurgery. In: proceedings of CVRMed-MRCAS'97, vol. 1205, pp. 467–476. Springer LNCS (1997)
37. Zhang, T.C., Grill, W.M.: Modeling deep brain stimulation: point source approximation versus realistic representation of the electrode. Journal of Neural Engineering **7**(6), 066,009 (2010)